The Statistics and Sensitivity of a Double-Gyre Model: The Reduced-Gravity, Quasigeostrophic Case

JOHN D. MCCALPIN

College of Marine Studies, University of Delaware, Newark, Delaware

(Manuscript received 30 April 1993, in final form 11 July 1994)

ABSTRACT

The sensitivity of the time-averaged circulation of an oceanic double-gyre model to variations in the model's parameters and forcing is studied. Unresolved low-frequency variability in the solution leads to statistical uncertainty in the estimates of the time-averaged quantities. The authors utilize bootstrap analyses of a number of multicentury integrations of a reduced-gravity, quasigeostrophic, eddy-resolving ocean model to estimate these statistical uncertainties. An analysis is then presented of the sensitivity of the system to variations in the strength and asymmetry of the wind forcing and to variations in several other physical and numerical parameters of the system. The bootstrap results enable us to estimate error bounds on these sensitivities. The physical measures of the system investigated include the means and variances of the total energy, the peak transport, the location of the separation point, and the penetration scale of the free jet.

1. Introduction

The rectangular basin, midlatitude, double-gyre model has proven to be an important "laboratory" in our efforts to understand the dynamics of the midlatitude, wind-driven ocean circulation. Numerical simulations of prototypical single- and double-gyre oceans have been used to study the effects of the addition of nonlinearity to the classical Stommel and Munk models (Bryan 1963; Veronis 1966), the influence of topography on the gyre-scale circulation (Holland 1973; Verron et al. 1987), the role of eddies in the oceanic circulation and fluxes (Holland 1978), the influence of nonuniform winds (Rhines and Schopp 1991; Verron and LeProvost 1991), and other topics. The sensitivity of ocean general circulation models to several parameters was reviewed by Haidvogel (1979). The particular question of the sensitivity of the penetration scale parameter was discussed in Holland and Schmitz (1985).

Essentially all of these projects have analyzed the results, at least in part, by making use of a separation of the solution into a time-independent "mean" field and a time-dependent "eddy" field. This form of analysis has been used to derive and define the mean and eddy transport streamfunctions, the mean and eddy heat fluxes, and the mean and eddy energetics and the associated energy transfers. Despite the extensive use of this separation into mean and fluctuating components, the statistics of this technique (in the context of wind-driven models) have not been previously addressed in the oceanographic literature.

Recent advances in computer performance have made it possible to revisit the simplest double-gyre model with runs 10–100 times longer than those previously reported. The long time series obtained from these simulations provide input for a bootstrap statistical procedure designed to infer the characteristics of the variabilities and statistical uncertainties of the "mean" and "eddy" quantities.

This report presents the results of an analysis of a particularly simple model: the reduced-gravity quasigeostrophic model operating in a rectangular domain with simple variations on the classical double-gyre wind forcing. This model was chosen as the simplest possible dynamical system containing the essential elements of Rossby waves, lateral shear instability, and damping (both bottom drag and lateral viscosity). The classical double-gyre forcing was chosen in order to provide a free jet analogous to the Gulf Stream.

The motivation for the project is a desire to understand the sensitivity of the climatologically relevant (i.e., time- and space-averaged) measures of midlatitude ocean flows to variations in several of the physical and numerical parameters of the simulation. Although this model does not contain heat transport, a variety of parameters (including the free-jet penetration scale, the total energy of the system, and the variability of the total energy) are likely to be closely related to the actual heat transport (and its variability) of more complete simulations.

Corresponding author address: Dr. John D. McCalpin, College of Marine Studies, University of Delaware, Robinson Hall, Newark, DE 19716-3501.

2. Model description

The model is an extension of that described (briefly) in McCalpin (1987).[1] The vertical structure of the fluid is assumed to be two immiscible, homogeneous layers of slightly different densities. The lower layer is assumed to be infinitely deep and at rest. The model integrates a standard second-order finite-difference approximation to the quasigeostrophic vorticity equation for the upper-layer flow

$$(\nabla^2 - \gamma^2)h_t + \beta h_x = \frac{g'}{f_0} J(h, \nabla^2 h) - r\nabla^2 h - A_b \nabla^6 h + \frac{f_0}{\rho_0 g' H} \operatorname{curl} \vec{\tau}, \quad (1)$$

where h is the interface anomaly (positive upward), r is the coefficient of interfacial friction, A_b is the coefficient of high-order (biharmonic) viscosity, τ is the wind stress on the ocean surface, ρ_0 is the mean density of seawater, and H is the reference thickness of the upper layer. The subscripts x and t indicate partial derivatives. Other definitions include

$$\gamma^2 = \frac{f_0^2}{g'H} = (47\,636)^{-2}\ \mathrm{m}^{-2},$$

$$g' = g\frac{\Delta\rho}{\rho_0} = 0.02\ \mathrm{m\ s}^{-2},$$

$$\beta = \frac{\partial f}{\partial y} = 1.97 \times 10^{-11}\ \mathrm{m}^{-1}\ \mathrm{s}^{-1},$$

$$J(a, b) = \frac{\partial a}{\partial x}\frac{\partial b}{\partial y} - \frac{\partial a}{\partial y}\frac{\partial b}{\partial x},$$

$$\nabla^2 a = \frac{\partial^2 a}{\partial x^2} + \frac{\partial^2 a}{\partial y^2},$$

$$\nabla^6 a = \nabla^2(\nabla^2(\nabla^2 a)).$$

In the above, f is the Coriolis parameter (assumed to be a linear function of y), $f_0 = 7.27 \times 10^{-5}\ \mathrm{s}^{-1}$ is the value of the Coriolis parameter at the middle of the domain, g is the gravitational acceleration, and $\Delta\rho$ is the difference between the layer densities. The Jacobian term is approximated using the nine-point energy- and enstrophy-conserving scheme of Arakawa (1966).

The governing equation (1) is solved in a domain of 3600 km (E–W) by 2800 km (N–S) extent, subject to several boundary conditions. The first is the "kinematic" boundary condition, which is simply the statement that there is no flow through the closed boundaries. The implication of this is that h must be constant along a closed boundary. The constant may be a function of time, however, and this extra degree of freedom is used to enforce global mass conservation (McWilliams 1977).

The second boundary condition is the specification of the viscous stress on the boundary due to the lateral viscous term. In all cases presented here a free-slip boundary condition is used. Additionally, the fourth normal derivative of the streamfunction is declared to vanish at the boundary. These conditions guarantee that there is no contribution to the integrated momentum budget due to viscous effects at the boundaries. For studies of the implications of the choice of the free-slip condition, see Haidvogel et al. (1992) and Chassignet and Gent (1991).

This choice of governing dynamics does have several drawbacks. Most notably, the reduced-gravity approximation eliminates the possibility of baroclinic instability [though the coarseness of the vertical representation here would reduce the baroclinic instability even if it were allowed by the equations (Adamec 1988, 1989)]. It was noted that no instability occurred in the reduced-gravity model of Holland and Lin (1975). Such a tendency was also noted in these experiments, but in the present work, the introduction of a small asymmetry to the wind field was effective in keeping the solution away from a symmetric, stable state.

The combination of weak biharmonic viscosity and free-slip boundaries can result in excessive velocities in the model (given the standard values of wind stress). Therefore, the model contains an ad hoc interfacial friction to limit the maximum velocities to $O(1)\ \mathrm{m\ s}^{-1}$ for the standard parameters. This viscous term damps the upper-layer relative vorticity excessively compared to the behavior of models with more accurate vertical representations and, in particular, causes eddies and rings to decay too fast. This energy loss in the upper layer acts as a very coarse analog to the downward energy flux (upper layer through barotropic mode to bottom friction) commonly found in these models, though without the proper dependence on scale and nonlinearity.

3. Statistics

The statistical analysis of time series is, of course, an immense field. The application of some basic statistical principles to the estimation of errors in the moments of oceanic observations is presented in Flierl and McWilliams (1977). The present work is intended to complement the traditional approaches based on covariance or spectral estimates, and attempts to infer (rather than assume) as much as possible about the statistics of the system.

A discussion of the dynamical basis of the low-frequency variability is deliberately omitted here. Though such a study is of considerable intrinsic interest, we are

[1] A 60-page technical report describing the model and containing the full source code is available from the author in either hard copy or machine-readable format.

here concerned with *averaging away* that low-frequency variability, rather than explaining it. For this purpose, the current methodology is adequate. It is relevant to note, however, that the low-frequency variability appears to be the result of two factors: 1) a simple (i.e., with a Gaussian distribution) randomness due to the generation of eddies and in their interactions with the free jet and western boundary currents and 2) a large enhancement due to the existence of persistent anomalous modes of the system in some parts of the parameter space. Two such anomalous states have been identified: a strongly penetrating jet with weak eddies, and a nonpenetrating jet with a very strong eddy field. These persistent states are most commonly observed in the region of parameter space close to that which yields steady solutions, and evidence for the existence of these states can be seen in the total energy histogram of the reference case (Fig. 12). The phenomenology of these anomalous states will be discussed in a separate manuscript. There is no evidence of large-scale basin modes or other quasi-linear phenomenon contributing to the low-frequency variability in total energy, though such modes are visible (but weak) in an EOF analysis of the variability of the streamfunction fields.

a. The bootstrap technique

The primary analysis technique employed here is a bootstrap, or subsampling, scheme that attempts to derive as much information as possible about the statistics of the series from the series itself. It does this by contrasting the statistical properties (mean and variance) of independent subsets of the series and treating them as a statistical ensemble of realizations from the solution space of the model. The discussion in this section is limited to the results for the total energy, but the same analysis is applied to obtain the sensitivity results for other measures of the system, discussed in section 4.

The basic procedure is as follows: the instantaneous total energy of the system was saved every five days for each of the runs (which are described in the next section). The first 10 years of data was considered to be contaminated by the spinup process and was discarded. This appears to be a conservative choice, since the model reaches the asymptotic total energy range in about 5 years. Beginning with the data at year 10, the series was truncated to the largest "convenient" number of samples, where convenient means that the sample length had a large number of small prime factors so that the subsamples could be of many different lengths. For example, the 200-year runs had 14 400 samples total, of which the first 720 were discarded. Of the remaining 13 680 samples, the first 13 500 were chosen for the analysis. The resulting series can be evenly divided into independent bins of lengths 2, 3, 4, 5, 6, 9, 10, 12, 15, 18, 20, 25, 27, 30, 36, 45, 50, 54, 60, 75, 90, 100, 108, 125, 135, 150, 180, 225, 250, 270, 300, 375, 450, 500, 540, 675, 750, 900, 1125, 1350, 1500, 2250, 2700, 3375, 4500, and 6750 elements. These contiguous bins correspond to averaging intervals of 10 days to approximately 90 years.

For each averaging interval, the mean and standard deviation of each subsample was calculated by

$$\overline{\mathrm{TE}}_j(T) = \frac{1}{k}\sum_{i=1}^{k} \mathrm{TE}_{(j-1)k+i}, \quad j = 1, \cdots, M/k, \quad (2)$$

$$\sigma_j(T) = \left(\frac{\sum_{i=1}^{k} (\overline{\mathrm{TE}}_j(T) - \mathrm{TE}_{(j-1)k+i})^2}{k-1}\right)^{1/2}, \quad j = 1, \cdots, M/k, \quad (3)$$

where T is the averaging interval in units of time, $k = T/\Delta t$ is the number of samples in the averaging interval (also called the bin length), M is the total number of data points, j is the bin number, and TE is the total energy. Note that the standard deviations are defined relative to each bin's mean, rather than to the global mean, since in any single realization only the sample mean will be known.

Next, for each averaging interval, the standard deviation of the set of mean estimates was calculated, $(\sigma(\overline{\mathrm{TE}}))$, as were the mean and standard deviation of the standard deviation estimates $[\overline{\sigma(\mathrm{TE})}$ and $\sigma(\sigma(\mathrm{TE}))]$. Note that the mean of the mean estimates is simply the global mean for the series and is, therefore, not a function of the averaging interval. The standard deviation of the mean estimates, $\sigma(\overline{\mathrm{TE}})$, is interpreted as the statistical uncertainty of the mean estimate for any single sample of length T. Similarly, the standard deviation of the standard deviation estimates, $\sigma(\sigma(\mathrm{TE}))$, is interpreted as the uncertainty in the "eddy energy" estimate for any single sample of that length. The mean of the standard deviation estimates, $\overline{\sigma(\mathrm{TE})}$, provides information about the bias in the average eddy energy estimates caused by the use of incorrect means. It also provides information about the stationarity of the system, since it must converge to a limit as the averaging interval goes to infinity if the system is stationary.

b. Variability of mean total energy estimates

For each numerical experiment, the function $\sigma(\overline{\mathrm{TE}})$ was examined and extrapolated (subjectively) to provide an estimate of the uncertainty in $\overline{\mathrm{TE}}$ for the full-length series. In most cases this provides values very similar to the difference between the two longest subsamples, but there are some cases for which this value had to be adjusted upward because the function dropped unreasonably fast between averaging intervals of one-third the full series length and one-half the series length. (See the curve for run 106 in Fig. 2 for an ex-

TABLE 1. Bootstrap statistics of the 12 standard test cases used in this study. All values are in units of 10^{16} J. Values marked with asterisks have been estimated by smoothing the relevant curve because the final value of the actual curve was observed to be anomalously low (e.g., see Fig. 2).

Run	$\overline{TE}$	$\sigma(\overline{TE})$	σ	$\sigma(\sigma)$	Comments
101	38.8	1.5	2.43	0.22	short time step
102	34.2	1.1	1.60	0.32	increased asymmetry
103	8.3	0.0	0.04	0.04	steady solution
104	39.0	0.9	2.64	0.02	reference case
105	102.0	1.8	8.30	0.93	strong winds
106	203.0	*4.0	15.80	1.08	very strong winds
107	33.0	0.1	0.99	0.12	strong asymmetry
108	43.6	0.2	1.68	0.52	no asymmetry
109	39.4	0.7	1.83	0.90	decreased viscosity
110	40.3	1.8	1.98	0.58	Δx = 10 km
111	36.7	0.2	2.51	0.05	Δx = 40 km
112	38.2	*0.5	2.40	0.20	very low viscosity

ample.) Numerically similar estimates were obtained for some of the cases by fitting a $1/\sqrt{T}$ curve to the function—see the discussion in section 3d or by equating $E(0)$ and T_0 via (5) in section 3d. Table 1 presents the values of $\overline{TE}$, $\sigma(\overline{TE})$, $\sigma(TE)$, and $\sigma(\sigma(TE))$ for each of the experiments, whose parameters are summarized in Table 2 in section 4.

Samples of the bootstrap curves for $\overline{TE}$ are presented in Fig. 1 for runs 108, 102, 104, and 107 (this is a sequence with increasing asymmetry parameter), and Fig. 2 for runs 104, 105, and 106 (a sequence with increasing wind stress curl magnitude). Note that the uncertainty in $\overline{TE}$ is not scaled by σ (the standard deviation of the entire series), but by the average standard deviation for samples of length T, $\sigma(T)$. This is a more helpful normalization for analyzing the results of short calculations, for which the asymptotic value of σ may not be known, and only the sample standard deviation is available.

c. *Statistics of the standard deviation estimates*

The average value of the standard deviation of the total energy is a strong function of the averaging interval. This is not surprising, since the shorter averaging periods are not able to capture the low-frequency variability as part of the variance, but lose it to the different estimated means for each bin. An example of the mean and standard deviation of the standard deviation estimates, $\overline{\sigma(TE)}$ and $\sigma(\sigma(TE))$, is presented in Fig. 3 for the reference case, run 104. This is one of the "best" cases, for which the uncertainty in the standard deviation estimates tends toward zero. A case displaying less desirable behavior is run 108, whose results are shown in Fig. 4. In this case the variability of the standard deviation is not showing an obvious tendency toward zero as the averaging interval increases. In most cases, the $\overline{\sigma(TE)}$ appears to approach an asymptotic value as the averaging interval increases to the total length of the series. This suggests that the systems are stationary—in agreement with the spectral estimates.

d. *Discussion of the statistics*

It is common practice to estimate the uncertainty in the mean estimate of a time series by an approximation such as

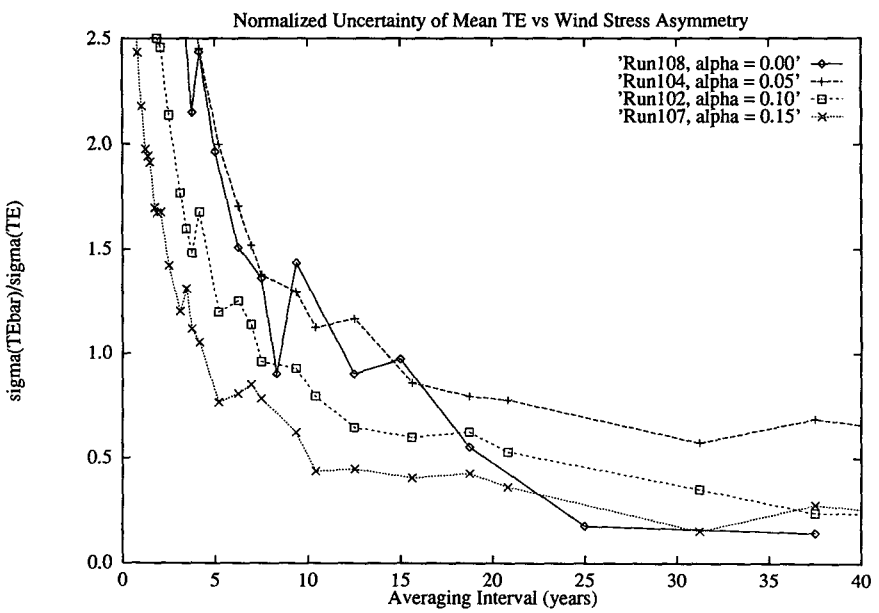

FIG. 1. Dependence of the standard deviation of the total energy, $\sigma(\overline{TE})$, on the length of the averaging interval and the asymmetry parameter α. See text for a discussion of the normalization.

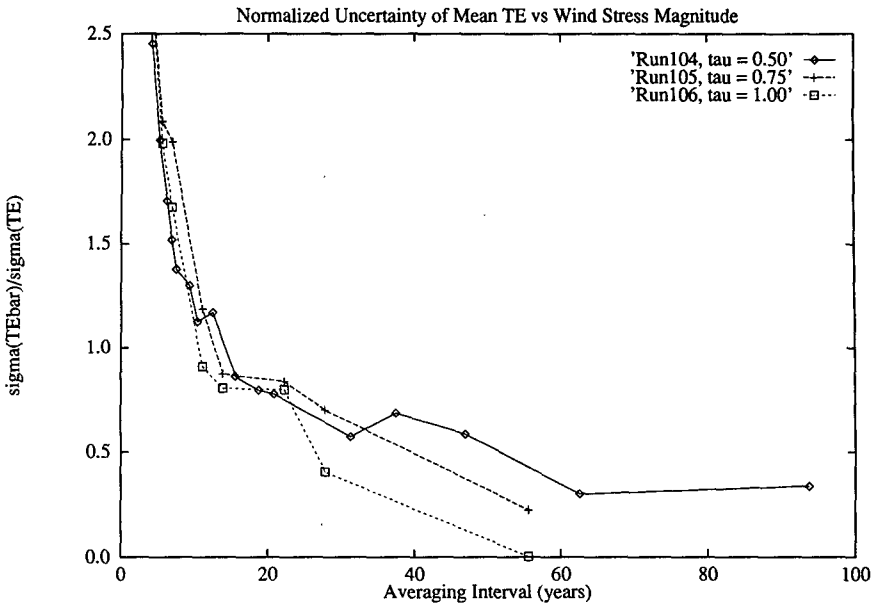

FIG. 2. Dependence of the standard deviation of the total energy, $\sigma(\overline{\mathrm{TE}})$, on the length of the averaging interval and the magnitude of the wind stress curl. See text for a discussion of the normalization.

$$\sigma(\overline{\mathrm{TE}}) \approx \sigma(\mathrm{TE}) \times \left(\frac{T_0}{T}\right)^{1/2}, \qquad (4)$$

where $\sigma(\mathrm{TE})$ is the sample standard deviation, T is the sample length, and T_0 is a "decorrelation timescale." This decorrelation timescale can be defined in a number of ways, including the time to the first zero crossing of the autocorrelation function, or the integral of the absolute value of the autocorrelation function. In all cases, the intent is to capture some measure of the low-frequency variability of the system into a single parameter. It is shown in Flierl and McWilliams (1977) that

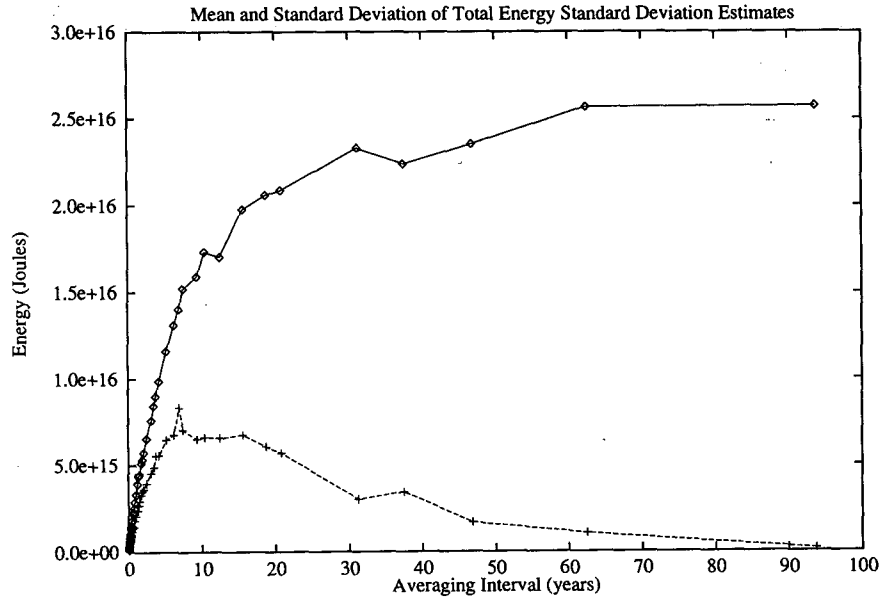

FIG. 3. Dependence of the mean of the standard deviations of the total energy, $\overline{\sigma(\mathrm{TE})}$, and the standard deviation of the standard deviations of the total energy, $\sigma(\sigma(\mathrm{TE}))$, on the length of the averaging interval for the reference case, run 104.

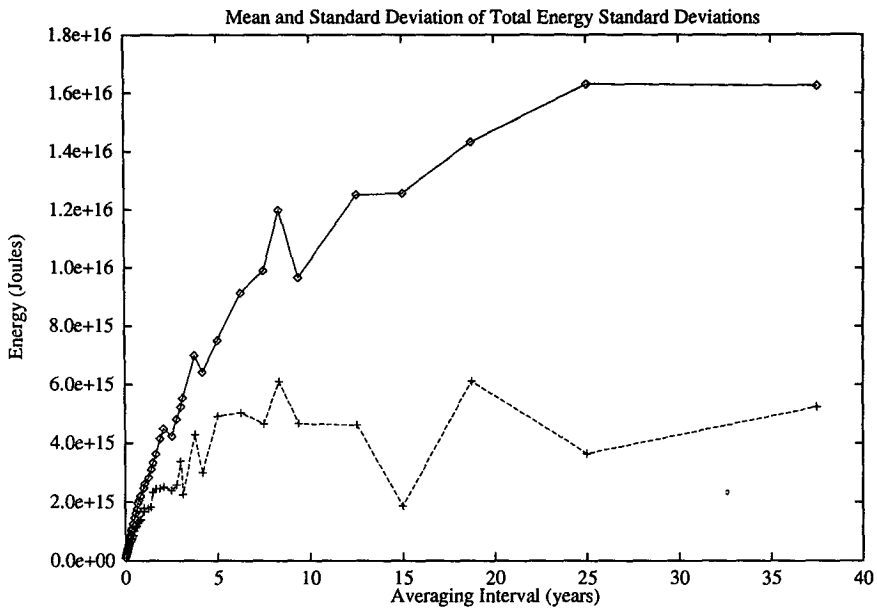

FIG. 4. Dependence of the mean of the standard deviations of the total energy, $\overline{\sigma(\mathrm{TE})}$, and the standard deviation of the standard deviations of the total energy, $\sigma(\sigma(\mathrm{TE}))$, on the length of the averaging interval for the symmetric wind case, run 108.

this is the first term of an asymptotic expansion (in $1/T$) for the exact expression for the error in the mean estimates. Their Eq. (2.16) is

$$\sigma(\mathrm{TE}) \approx \left(\frac{2\pi E(0)}{T}\right)^{1/2} \equiv \left(\frac{2\sigma^2 T_0}{T}\right)^{1/2}. \quad (5)$$

For comparison with the bootstrap results of this study, two definitions of the decorrelation timescale T_0 were chosen, patterned after the definitions above. Specifically, τ_0 is defined as the time to the first zero of the autocorrelation function, and τ_1 is defined as

$$\tau_1 = \int_0^{T/2} |\alpha(\tau)|\, d\tau, \quad (6)$$

where α is the autocorrelation function

$$\alpha(\tau) \equiv \frac{\displaystyle\int_0^{T-\tau} \mathrm{TE}(t)\mathrm{TE}(t+\tau)dt}{\left(\displaystyle\int_0^{T-\tau} \mathrm{TE}^2(t)dt\right)^{1/2} \times \left(\displaystyle\int_\tau^{T} \mathrm{TE}^2(t)dt\right)^{1/2}}; \quad (7)$$

in other words, τ_1 is defined as the integral of the absolute value of the autocorrelation function for lags from 0 to $T/2$.

A comparison of several approaches (bootstrap, $T_0 = \tau_0 = 21.39$ years, and $T_0 = \tau_1 = 15.35$ years) for run 104 is presented in Fig. 5. The bottom curve is normalized by σ, as suggested by (5). The next curve is normalized by $\sigma(\overline{\mathrm{TE}})/\overline{\sigma(\mathrm{TE})}$—in other words, the standard deviation among the mean total energy estimates was scaled by the average standard deviation among the samples of that length. The two upper curves are based on (4) with the two choices of decorrelation timescale mentioned above. The normalization by the mean standard deviation for each averaging interval results in a much better correlation between the upper curves and the bootstrap results.

The quantitative correspondence of the estimates for this particular run is one of the highest for all of the experiments. For this case, all three versions give results with variations of less than 25% between the estimates of $\sigma(\overline{\mathrm{TE}})$ for most averaging periods. For other cases (not shown), the estimates of $\sigma(\overline{\mathrm{TE}})$ differ by factors of up to 3. Unfortunately, even in this "best" case (run 104), the τ_0 and τ_1 estimates were based on decorrelation scales calculated for the entire 190-year dataset. It is clear that a run much longer than 15–20 years would be necessary to correctly estimate a decorrelation timescale in the 15–20-year range. By necessity, a 10-year run (for example), would not be able to estimate a decorrelation timescale in excess of about 3 years. (Since the mean is removed before calculating the autocorrelation function, its integral over the sample length must vanish. This sets a strong constraint on the allowable T_0 measures of the function.) If this value were used for T_0, the estimates of the uncertainty in $\overline{\mathrm{TE}}$ would be severely biased downward. In addition, the scaling of the uncertainty is by the *mean* standard deviation for each averaging length, not the sample standard deviation for each sample. Since $\sigma(\mathrm{TE})$ has

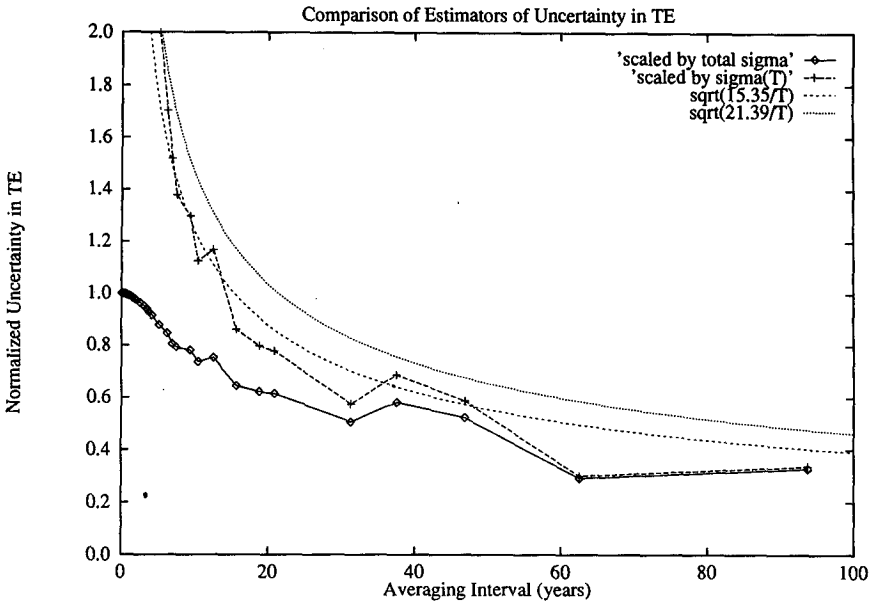

FIG. 5. Comparison of three different methods for estimating the uncertainty in the mean estimate for run 104. The curves show the results for the bootstrap technique as well as for two different estimates based on the decorrelation timescale of the entire 190-year series. For each averaging interval, the standard deviation of the mean total energy estimates was scaled by the average standard deviation for the samples of that length.

already been shown to have a great deal of variability (e.g., see Figs. 3 and 4 for averaging periods of less than 10 years), an estimate of $\sigma(\overline{\mathrm{TE}})$ based on $\sigma(\mathrm{TE})$ rather than $\overline{\sigma(\mathrm{TE})}$ can be expected to be subject to large uncertainty itself.

An attempt was made to estimate T_0 by least-squares fitting a curve of the form of (4) to the bootstrap results, but the results were not satisfactory for many of the cases. The detailed structure of the curve for the bootstrap technique in several cases differed substantially from the $1/\sqrt{T}$ form of (4), so that the fitted curve (not shown) deviated too much from the bootstrap data at either short or long T to be a fair representation of the bootstrap data. If it was chosen to fit the structure of the bootstrap curve for long T, then (unlike run 104) the best fit T_0 could be as much as a factor of 3 different than either τ_0 or τ_1. If it was chosen to fit the structure of the bootstrap curve for short T, then the estimates for the uncertainty in $\overline{\mathrm{TE}}$ could be off by as much as a factor of 3.

COMPARISON WITH SPECTRAL ANALYSIS

Although the analysis here is not directly concerned with estimates of the spectrum of the variability of the total energy, some understanding of the shape of the spectra is crucial to understanding both the system and the reliability of the statistical analysis techniques employed. Figure 6 provides an estimate of the spectrum of the variability of the total energy series from the reference case, run 104. This spectrum is based on about 990 years of model output sampled at 5-day intervals. The spectral estimation was performed by the MATLAB™ routine SPECTRUM, with a window length of 7200 samples (100 years) and a Hanning filter on each window. The 95% confidence intervals shown are based on the variations among the 10 win-

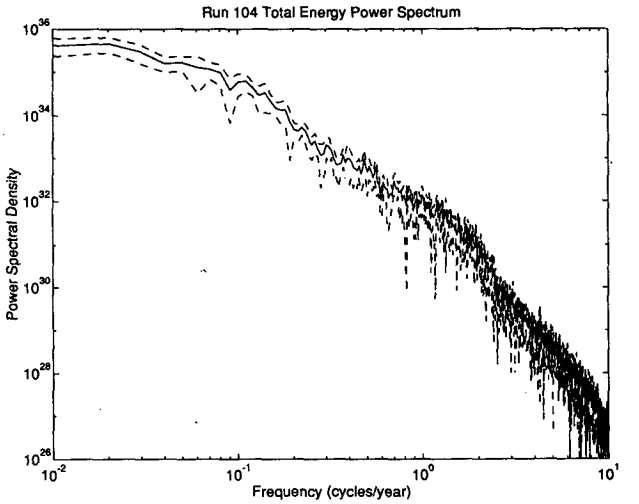

FIG. 6. Estimate of the power spectrum of the variability of the total energy from run 104 with 95% confidence intervals. The low-frequency end of the spectrum shows a level spectral energy density for all frequencies below about 0.05 cpy, including the next decade below that shown in this figure.

TABLE 2. Parameters of the 12 test cases used in this study. All cases employed the same basin geometry (3600 km × 2800 km) and bottom drag coefficient of 10^{-7} s^{-1}, and unless otherwise specified, used Δx = 20 km, Δt = 7200 s, and averaged adjacent time levels (equivalent to a forward time step) every NAVG = 99 steps. τ^x is the magnitude of the wind stress in dyne cm^{-2}, α is the asymmetry parameter, A_b is the lateral hyperviscosity parameter, and T is the length of the integration.

Run	τ^x	α	A_b	T (years)	Comments
101	.50	.05	8×10^{10}	90	Δt = 3600 s, NAVG = 999
102	.50	.10	8×10^{10}	200	moderate asymmetry
103	.25	.05	8×10^{10}	138	weak winds, NAVG = 999
104	.50	.05	8×10^{10}	200	reference case
105	.75	.05	8×10^{10}	125	strong winds
106	1.00	.05	8×10^{10}	125	very strong winds
107	.50	.15	8×10^{10}	200	strong asymmetry
108	.50	.00	8×10^{10}	200	no asymmetry
109	.50	.05	2×10^{10}	200	decreased viscosity
110	.50	.05	2×10^{10}	100	Δx = 10 km
111	.50	.05	2×10^{10}	200	Δx = 40 km
112	.50	.05	5×10^{9}	200	very low viscosity

dows. The spectrum appears roughly flat below a frequency below 0.1 cpy and falls off rather quickly at higher frequencies. The high-frequency end is biased by spectral leakage in this example, but it is the low-frequency variability that is expected to control the statistics of time averages.[2] The evidence is strong that the spectrum is flat for all frequencies below about 0.05 cpy, but the error bars of the spectral analysis widen considerably at lower frequencies. Very similar spectra were obtained for all the other runs analyzed here as well. All appear to have cutoff periods of about 0.1 years, but there were quantitative differences in the value of the low-frequency asymptote of the spectral energy density.

Some aspects of the statistics and consequences of various spectrum shapes are discussed in Wunsch (1992). Wunsch notes that there is no guarantee that the climate system is stationary because we do not know anything about the low-frequency limit of the spectral energy density. The power spectrum shown in Fig. 6 suggests that the system modeled here is, in fact, stationary. The shape of the curve in that figure suggests that we model the power spectrum as

$$P(\omega) = P(0)\frac{1}{1 + (\omega/\omega_0)^n}, \qquad (8)$$

where P is the power spectral density, ω is the frequency normalized by the "cutoff" frequency of a low-pass filter, and n is the order of the filter. In this case, the cutoff frequency is apparently about 0.1 cpy, and the order is about 5–6. The variance of a time series governed by such a spectrum is finite, so that the system is stationary, and the analysis of Flierl and McWilliams (1977) is applicable to the estimation of errors in mean and standard deviation estimates.

As mentioned previously, the power spectral density of the low-frequency plateau can be converted to the equivalent first-order [in $(1/T)$] asymptotic approximation for the estimated error in the mean [Flierl and McWilliams (1977), Eq. (2.16)]

$$\sigma(\mathrm{TE}) \approx \left(\frac{2\pi E(0)}{T}\right)^{1/2}. \qquad (9)$$

For the scaling conventions used in the calculation of Fig. 6 [$E(0) = P(0) \times (T/N)$, where N is the number of elements in the series], this gives

$$\sigma(\mathrm{TE}) = \left(\frac{2\pi P(0)}{N}\right)^{1/2} \approx 1.2 \times 10^{16}\ \mathrm{J}. \qquad (10)$$

This estimate of the uncertainty in estimates of $\overline{\mathrm{TE}}$ agrees rather well with the bootstrap result of 0.9×10^{16} J for this run.

4. Sensitivity

Several series of experiments were performed to investigate the sensitivity of the time-averaged model solution fields to variations in the wind forcing and other parameters. A central set of parameters was chosen as the reference case (run 104). These were chosen (subjectively) to provide the most "realistic" simulations, with peak velocities of approximately 0.8 m s^{-1}, and a meandering eddy-generating free jet. The values of the parameters for all the cases are presented in Table 2.

a. Dependence on wind stress curl symmetry

A total of four values of the wind stress curl asymmetry parameter, α, were used, with values of 0.0, 0.05, 0.10, and 0.15. These values define the distribution of the wind stress curl according to

[2] The small "shoulder" at 1–2 cpy is real, and results from a preferred period of eddy–jet interactions, which are far more obvious in spectra of the amplitudes of the EOFs of the streamfunction variability (not presented here).

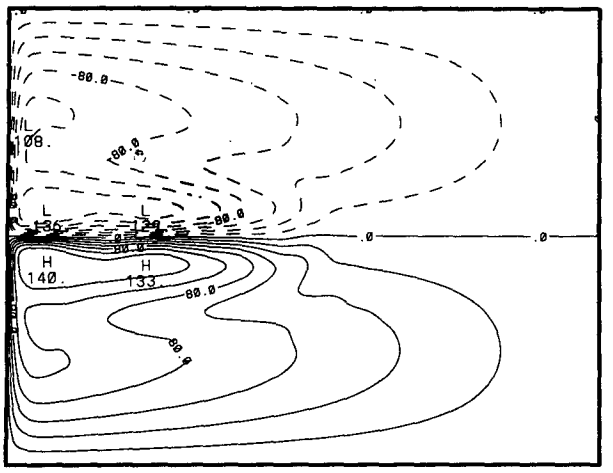

FIG. 7. Time-averaged upper-layer thickness anomaly for the case of perfectly antisymmetric winds (run 108, $\alpha = 0.00$).

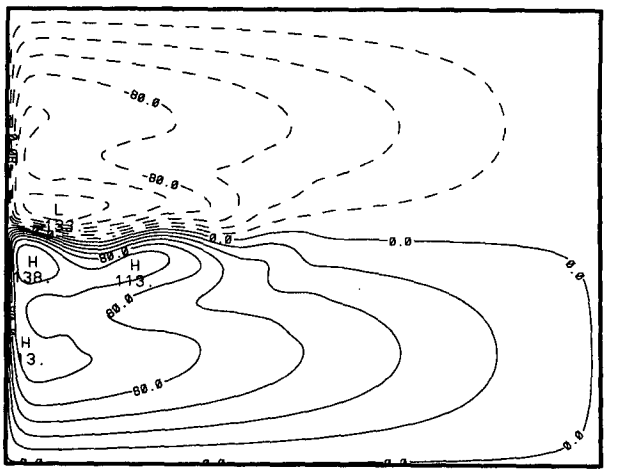

FIG. 8. Time-averaged upper-layer thickness anomaly for the reference case with mildly asymmetric winds (run 104, $\alpha = 0.05$).

$$\tau^x(y) = \tau_0 \sin(2\pi y)\left[1 - 4\alpha\left(y - \frac{1}{2}\right)\right], \quad (11)$$

where $0 < y < 1$ is the normalized meridional position relative to the southern boundary of the system. This form of asymmetry was chosen to force the solutions to mimic the effect of varying layer depth in the advection of relative vorticity term, which is ignored in the quasigeostrophic approximation. For the reference value of 0.05, the peak wind stress curl in the subtropical gyre is increased by 5% and the peak wind stress curl in the subpolar gyre is decreased by 5%. Values of α of the order of the Rossby number should be expected to provide a good simulation of the effect of varying layer thickness in a more dynamically complete model, and in fact, $\alpha = 0.05$ results in mean streamfunction patterns very similar to those obtained from the linear balance equations by McWilliams et al. (1990), which are, in turn, very similar to those for the primitive equations.

Figures 7, 8, and 9 show the time-averaged upper-layer thickness anomaly fields for α values of 0.00, 0.05, and 0.15, respectively. The symmetric wind case produces a symmetric time-averaged solution, as expected, while increasing α results in an overshooting of the southern branch of the western boundary current past the line of zero wind stress curl.

Applying the bootstrap analysis to the instantaneous values of the maximum streamfunction reveals that the maximum transport (which is always in the southern gyre because of the wind asymmetry) increases in exact proportion to the maximum of the southern gyre wind stress, from 27.7 Sv (Sv $\equiv 10^6$ m^3 s^{-1}) for $\alpha = 0$ to 31.4 Sv for $\alpha = 0.15$. The standard deviation of the peak transport increases from ± 1.4 Sv to ± 2.4 Sv over the same range of α. Unfortunately, the model is not dynamically complete enough to obtain a realistic barotropic recirculation, so this measure will not be further discussed here except to note that the time averages of the peak transport converged to their asymptotic values in a manner quantitatively similar to the total energy.

Figure 10 shows that $\overline{\text{TE}}$ is a weak but significant function of α. The standard deviation, σ(TE), is a more interesting function of α, as shown in Fig. 11. The variability of total energy has a clear and apparently statistically significant maximum for $\alpha = 0.05$, with lower values for either more symmetric or more asymmetric winds. Although the precise dynamical explanation for this dependence is not completely clear, it appears that intermediate values of α provide an "optimum" amount of asymmetry to the system. This leads to the creation of large amplitude meanders and rings during

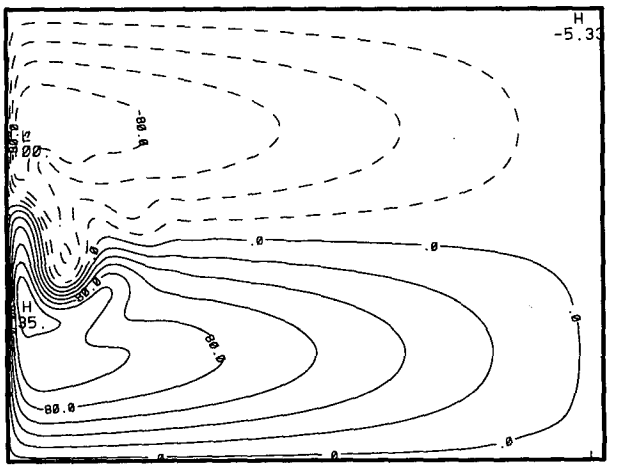

FIG. 9. Time-averaged upper-layer thickness anomaly for the case with strongly asymmetric winds (run 107, $\alpha = 0.15$).

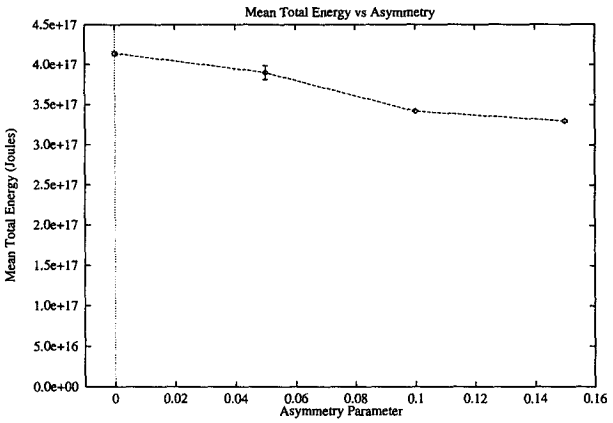

FIG. 10. Dependence of $\overline{\text{TE}}$ on the asymmetry parameter α, with error bars estimated by the bootstrap technique.

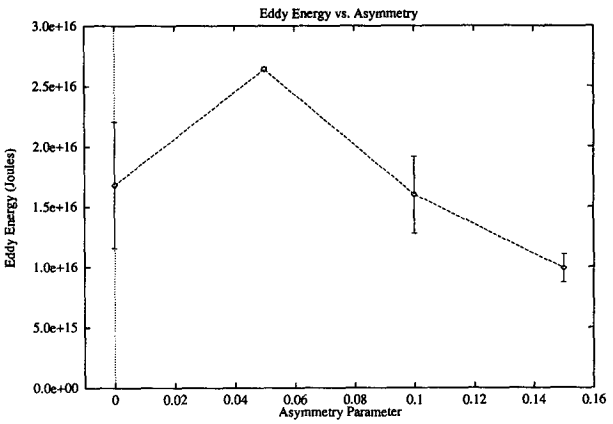

FIG. 11. Dependence of of the total energy variability, σ(TE), on the asymmetry parameter α, with error bars estimated by the bootstrap technique.

some periods, but still allows a quasi-steady (high energy) solution during other periods. Larger values of α result in a system with more-or-less continuous ring creation, and fewer periods of strong penetration (and associated high energy). Smaller values of α result in a system with insufficient perturbations to generate strong meanders and eddies, and therefore fewer periods of weak jet penetration and low energy.

Unlike the case where the magnitude of the wind stress is varied (as discussed in a later section), varying the asymmetry parameter appears to have a strong effect on the effective decorrelation timescale. This is clear from a comparison of Figs. 1 and 2. Unfortunately, a best-fit $1/\sqrt{T}$ curve gives an estimated decorrelation timescale as much as a factor of 3 smaller than either τ_0 or τ_1, as discussed in section 3d.

Another approach to visualizing the dependence of $\overline{\text{TE}}$ on α is by use of histograms of the distribution of total energy. Figure 12 shows the distribution of instantaneous total energy values for runs 104 and 107, with values of α of 0.05 and 0.15, respectively. Note that the distribution for run 104 has clear secondary peaks at both high and low energy, whereas the distribution for run 107 is nearly Gaussian. The peaks of the distributions are clearly separated, and there is relatively little overlap between the probability distribution functions. The situation is less clear comparing runs 102 and 107, with α values of 0.10 and 0.15, respectively. Figure 13 shows substantial overlap in the distributions of total energy, with peaks separated by an amount smaller than the standard deviations of either of the distributions, but greater than the bootstrap estimates of the uncertainties of either of the mean estimates.

1) PENETRATION SCALE

A commonly used measure of the midlatitude double-gyre system is the free jet's "penetration scale." A review of the literature shows that at least four independent definitions of penetration scale are in current use, of which most are quantitative, but one is only semi-quantitative. The quantitative definitions of penetration scale fall into two families: those based on distances to mean streamlines, and those based on distances to mean isotachs. Examples of the former include Marshall and Marshall (1992), who used the distance to the most eastward location of the 10% streamfunction contour, and Barnier et al. (1991), who used the eastward penetration of the zero streamfunction contour in the lowest layer of a multilayer model. An example of the latter definition is Haidvogel et al. (1992), who used the distance to the 16% isotach along the zero streamline. Other important papers in the area do not attempt fully quantitative definitions, including

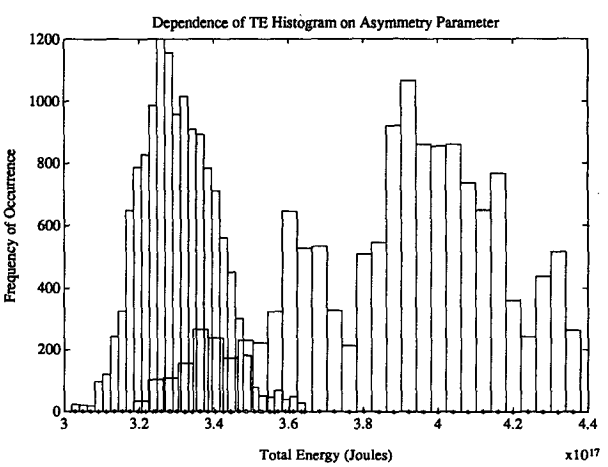

FIG. 12. Histogram of the distribution of total energy values for asymmetry parameters of 0.15 (left) and 0.05 (right). The distributions are well separated.

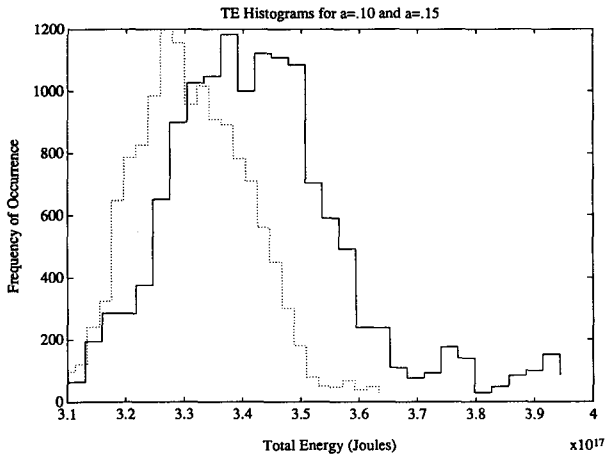

FIG. 13. Histogram of the distribution of total energy values for asymmetry parameters of 0.15 (left) and 0.10 (right). The distributions show substantial overlap, and the means differ by less than their standard deviations but more than their estimated uncertainties.

Holland and Schmitz (1985), where a visual inspection of the contours of eddy KE density is employed. The implications of the choice of definition on the dynamical interpretation of the problem are not always clear, but some comments can be made.

First, and most relevant to the work at hand, all of the measures depend on the separation of the streamfunction field into "mean" and "eddy" components. This introduces a significant statistical uncertainty into the results, which will be explored in appendix A. Second, measures based on distances to mean streamlines may be rather insensitive to the details of the actual free jet dynamics if the eastward end of the streamline contour chosen is in the Sverdrup interior, rather than in the recirculation region. Third, measures based on distances to particular isotach contours introduce an extra uncertainty based on the sensitivity of the measure to the choice of the specific contour. This is addressed briefly in appendix A. Fourth, definitions based on eddy KE provide no estimate in the case of steady flow, making direct comparisons of steady and unsteady solutions difficult.

Although all of these definitions have been used successfully in prior work, a new definition is introduced here. In keeping with the desire to develop a statistically robust analysis of the system, the definition of penetration scale used here is the first moment in x of the KE density. This definition has the advantage of containing no user-selectable parameters, and requires no time averaging of the streamfunction before it can be applied. Of course, the time series of instantaneous moments can be filtered or averaged as desired, but the existence of the time series provides adequate information for the estimation of the statistical uncertainty of the mean estimate via bootstrap or spectral techniques. Such estimates are not available using the standard techniques. A detailed comparison of the properties of the standard definitions and the first moment of the KE density is presented in appendix A.

In the double-gyre model, the variability of the first moment of the KE density in the x direction is very highly correlated with the variability of total energy in all of the runs tested. This correlation is because the bulk of the energy in the system is potential energy, and this potential energy is concentrated in the deep (shallow) pools of upper-layer water on the south (north) sides of the free jet. For a strongly penetrating jet, the model has both a large first moment of the KE density and large pools of potential energy in the sidelobes of the jet. For a weakly penetrating jet, the model has a small first moment of the KE density and much smaller pools of potential energy in the sidelobes of the jet. Because the mean values of total energy and penetration scale are quite different relative to their respective variability, the sensitivity of the mean value of the penetration scale is significantly stronger than the the sensitivity of the mean total energy, decreasing from 800 to 400 km as the asymmetry parameter is increased. This dependence of the penetration scale on α is presented in Fig. 14. The results are in qualitative agreement with those of Rhines and Schopp (1991), who introduced asymmetry by rotating the wind field so that the line of zero wind stress curl was not exactly zonal. A set of experiments somewhat more similar to the current work are those of Verron and LeProvost (1991), in which the wind stress curl was of unequal amplitude and zonal extent in the two gyres. They comment that the penetration scale is not strongly affected by the introduction of various asymmetries to the wind stress curl field, but they do not quantify this measure, so it is difficult to compare the results.

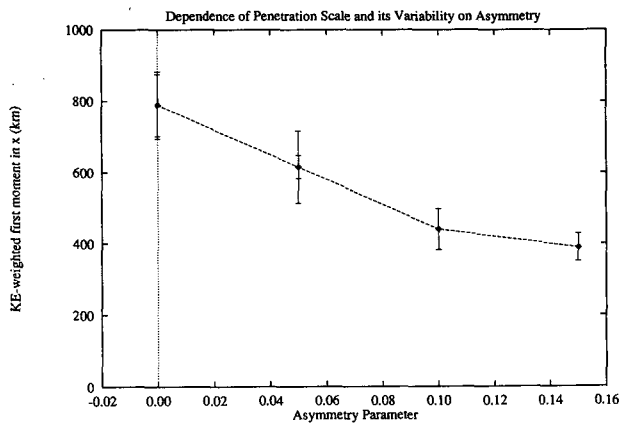

FIG. 14. Dependence of the KE-weighted first moment in x and its variability on the wind asymmetry parameter, α. The inner set of error bars shows the estimated uncertainty in the mean, while the outer set of error bars shows the standard deviation of the moment.

2) SEPARATION POINT

The determination of the dynamical controls on the location of the separation point of the free jet is a topic of considerable current interest. Here a very simple estimate of the free jet separation point is used: the separation point is assumed to be the y location of the maximum zonal velocity across a meridional line 60 km offshore. The bootstrap analysis enables the estimate of statistical uncertainties in the calculation of the mean separation point and in the calculation of the variability of the separation point.

The sensitivity of the separation point to the wind asymmetry parameter is documented in Fig. 15. Both location and standard deviation of the separation point are roughly linear functions of α. Unlike the case for the total energy, penetration scale, and maximum transport, the spectrum of the separation point variability is strongly peaked in these runs, with a maximum near 1-year periods. As a consequence, averaging periods of 2–3 years are adequate to obtain accurate estimates of the mean location and variability of the separation point.

The experiments of Rhines and Schopp (1991), using a rotated wind field, show a similar northward movement of the separation point as the integrated wind stress curl in the southern gyre is increased and the integrated wind stress curl in the northern gyre is decreased. An attempt to provide a formula predicting the separation point for various wind stress curl configurations is provided by Verron and LeProvost (1991), based on their QG model results with one, two, and three layers. Although the asymmetry of the wind stress curl used here is not of the exact family that they used, their formulas may still be approximately correct. Eliminating the terms that are held constant in the current experiments, their formula predicts that

$$\frac{L_N - L_S}{L_N + L_S} = \frac{\tau_N - \tau_S}{\tau_N + \tau_S}, \tag{12}$$

where L_S is the distance from the southern boundary to the separation point and L_N is the distance from the northern boundary to the separation point. Using the geometry of these experiments thus predicts a northward shift of the separation point of $y = 1400\alpha$, while the experiments show shifts of only 60% of this amount. This difference can likely be explained by the differences in the structure of the wind stress curl fields between the current experiments and theirs.

b. Dependence on wind stress curl magnitude

To examine the dependence of the time-averaged solutions on the magnitude of the wind stress, another series of experiments was run. A total of four values of wind stress magnitude were used, with nominal values of 0.25, 0.50, 0.75, and 1.00 dyn cm^{-2}. The series of runs numbered 103, 104, 105, and 106 form a series with increasing wind stress magnitude and all other parameters fixed. In particular, the asymmetry parameter is a fixed value of 0.05 for this series. The run with the weakest forcing displayed a nearly steady solution after the initial spinup transients.[3] This behavior appears to be due to the absence of baroclinic instability and has been previously noted in a reduced-gravity model by Holland and Lin (1975), but note that their experiments employed a single-gyre wind field. The other three cases all experienced vigorous barotropic instability and eddy generation.

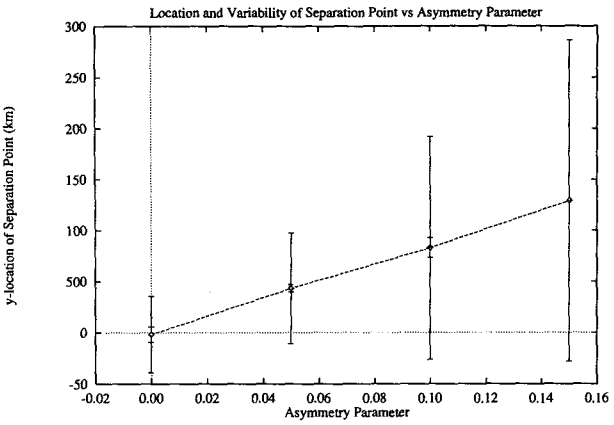

FIG. 15. Dependence of the mean y location of the separation point and its variability on the wind asymmetry parameter. The inner set of error bars indicates the statistical uncertainty of the mean estimate, while the outer set of error bars shows the standard deviation of the value.

The mean streamfunction fields for runs 105 and 106 are very similar to that of run 104 (but with significantly increased transport), and so are not shown here. The primary differences are a spreading out of the jet's streamfunction contours near the separation point (suggesting an increase in the variability of the location of the separation point with increasing nonlinearity) and a slight apparent increase in the penetration of the free jet. Peak transports in the southern gyre are 23, 30, and 44 Sv for runs 104, 105, and 106, respectively.

Both $\overline{\text{TE}}$ and $\sigma(\text{TE})$ are approximately quadratic functions of the wind stress curl magnitude for these cases (see Table 1). A more interesting quantity is the fractional energy variability, $\sigma(\text{TE})/\overline{\text{TE}}$, shown in Fig. 16. This quantity appears approximately constant for the three unstable cases, suggesting that at least this aspect of the instability is not sensitively dependent on the degree of nonlinearity of the system.

[3] Some linear Rossby waves were present in the solution but they did not affect the total energy to a detectable level.

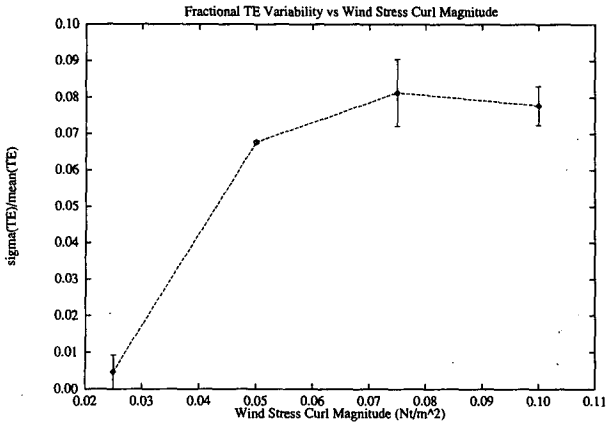

FIG. 16. Dependence of the fractional variability of total energy on the magnitude of the wind stress curl. Error bars are based on the bootstrap estimates of the error in the standard deviations.

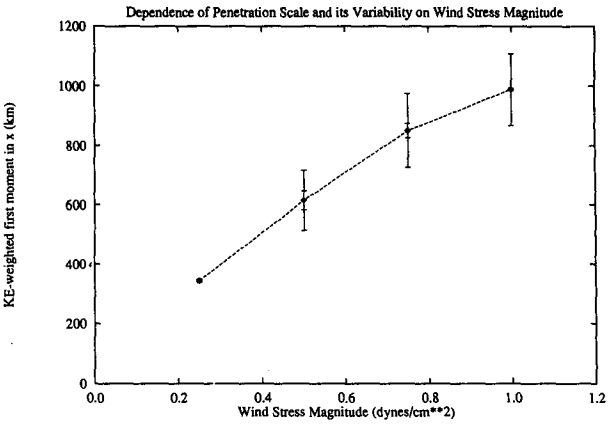

FIG. 17. Dependence of the penetration scale (KE-weighted first moment in x) on the magnitude of the wind stress. The inner set of error bars indicates the uncertainty in the mean estimates, while the outer set of error bars shows the standard deviation of the value.

Note, however, that this model is limited to quasigeostrophic dynamics, and the Rossby numbers present in the strongest two cases are O(1) in the western boundary and free jet region. Therefore this relative insensitivity to the strength of the forcing may be a limitation of the dynamical approximation rather than a more general characteristic of forced geophysical turbulence. A possibly related result is exhibited in Fig. 2, which shows that the apparent decorrelation timescale is largely independent of the amplitude of the wind stress curl, at least for averaging periods less than about 30 years. This result could be useful for estimating the uncertainty using (4) for series involving some shorter runs.

As was noted in the comments above on the mean streamfunction fields, there is an increase in the penetration scale with increasing wind stress. Figure 17 shows the increase to be slightly slower than linear, ranging from just over 300 km for the case with weakest winds to approximately 1000 km for the case with the strongest winds. The variability of the penetration scale is roughly independent of the wind stress magnitude for the three cases with eddy-generating solutions.

For the case of perfectly antisymmetric winds, the mean location of the separation point is expected to remain at the line of the zero of the wind stress curl ($y = 0$). For this series, however, the winds have a slight deviation from antisymmetry ($\alpha = 0.05$), so the the separation point is somewhat north of $y = 0$. As shown in Fig. 18, there is a joint effect of the nonlinearity and wind stress asymmetry, which produces a separation point that is a weakly increasing function of the wind stress magnitude. The northward shift is only 60 km, however, compared to the 120-km shift produced by the variation of the wind asymmetry parameter. A more significant change is the doubling of the standard deviation of the location of the separation point from ± 50 km to ± 100 km as the wind is doubled from 0.5 to 1.0 dyn cm^{-2}. This increased variability is evident in the mean streamfunction fields as a spreading out of the streamfunction contours near the mean separation point.

c. *Dependence on lateral hyperviscosity*

The lateral viscosity used in the model is of the hyperviscous form, proportional to the biharmonic operator on the relative vorticity. This form is in common use and was chosen because it is strongly scale selective, allowing relatively inertial solutions even with modest resolution. The value 8×10^{10} m^4 s^{-1} was chosen as the reference value, as it produces a Munk layer scale of one grid interval. Three experiments were run with

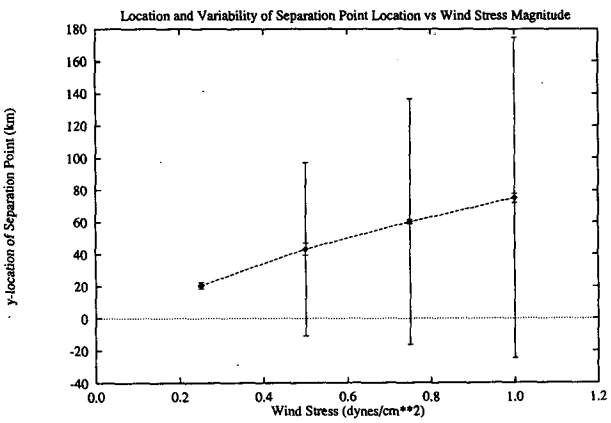

FIG. 18. Dependence of the mean y location of the separation point and its variability on the wind stress magnitude. The inner set of error bars indicates the statistical uncertainty of the mean estimate, while the outer set of error bars shows the standard deviation of the value.

TABLE 3. Variation in statistics due to changes in lateral hyperviscosity. All energies and standard deviations of 10^{16} J.

Run	A_b	$\overline{TE}$	$\sigma(\overline{TE})$	σ	$\sigma(\sigma)$
104	8×10^{10}	39.0	.87	2.64	.06
109	2×10^{10}	39.4	.74	1.83	.90
112	5×10^{9}	38.2	.75	2.40	.50

1/4 of that value, and one experiment used 1/16 of the reference value. Runs 104, 109, and 112 form a sequence with identical parameters except for the hyperviscosity parameter, which decreases by a factor of 4 from one run to the next. Visual inspection of the instantaneous relative vorticity fields showed that run 104 had smooth solutions, run 109 had a detectable amount of noise, and run 112 had a noisy solution. Despite this difference, neither $\overline{TE}$ nor $\sigma(TE)$ showed statistically significant variations. This weak dependence is consistent with the choice of parameters that makes bottom friction, rather than lateral friction, the dominant energy sink in the system. The results are summarized in Table 3.

In contrast to the small variations in $\overline{TE}$, the penetration scale estimates showed significantly different values, but with no obvious pattern. The three runs gave mean penetration scale values of 600, 775, and 620 km, respectively, with maximum uncertainties of no more than ±30 km. It is not clear if this difference is due to dynamical or numerical differences between the runs, since both of the reduced-viscosity runs had visible levels of noise in the relative vorticity fields.

The separation point showed a statistically significant migration northward of about 30 km as the viscosity was decreased. The standard deviation of the location of the separation point was significantly increased only for the (noisy) case with the smallest value of viscosity.

d. Dependence on discretization parameters

The model contains two discretization parameters whose influence on the solution is of interest. Comparison of the results of run 101 with the reference case (run 104) showed that there was no change in either $\overline{TE}$ or $\sigma(TE)$ when changing the time stepping parameters of the model by a factor of 2 (see Table 1). The model was not run with longer time steps because of a (linear) stability limit on the viscous terms, which are treated explicitly. This leaves the horizontal grid resolution as the primary numerical parameter of interest. Runs 111, 109, and 110 form a sequence with identical parameter except that the grid resolution varied from 40 to 10 km, with a reference value of 20 km. The time step was adjusted linearly to maintain a constant Courant number for the sequence.

The sensitivity of $\overline{TE}$ to Δx is shown in Fig. 19. Runs 109 and 110 had smooth solutions, while run 111 had significant (but not catastrophic) noise in the relative vorticity field. The difference between $\Delta x = 10$ km and $\Delta x = 20$ km may not be significant by itself, but the continued decrease in $\overline{TE}$ as the grid is increased to $\Delta x = 40$ km suggests that the difference is real. The dependence of $\sigma(TE)$ on Δx is shown in Fig. 20. The error bars in this case are much larger (note that the scale of the ordinate extends to zero in this case), and there is no evidence of statistically significant systematic variation.

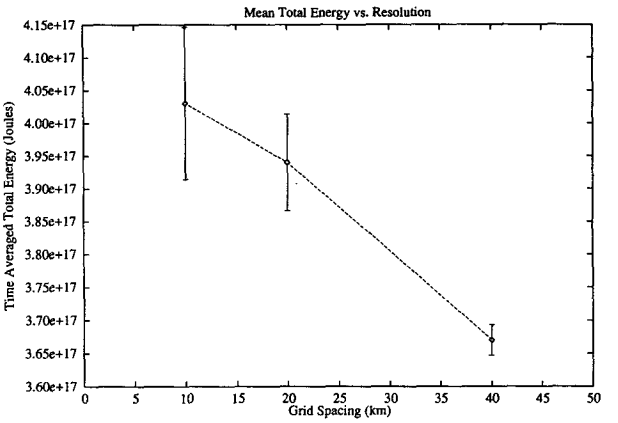

FIG. 19. Dependence of the mean total energy on the horizontal grid resolution.

The penetration scale in this series exhibited the same features as the total energy, with a statistically significant increase as the grid spacing was decreased. The location of the separation point showed the same trends, with mean values of 30, 65, and 70 km as the grid resolution was decreased. Both the change in mean location of the separation point and change in the standard deviation of the location of the separation point were significant between $\Delta x = 40$ km and

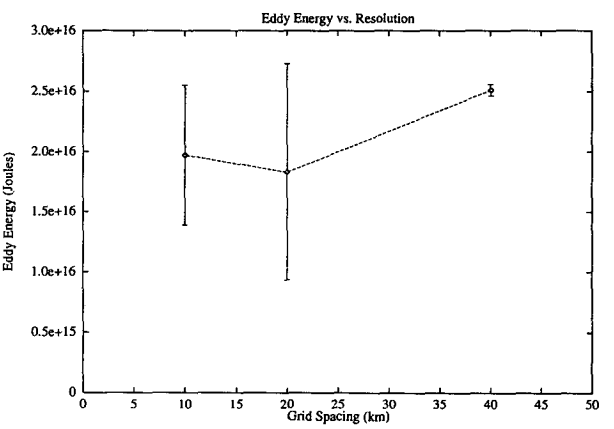

FIG. 20. Dependence of the standard deviation of the total energy on the horizontal grid resolution.

Δx = 20 km, but not between Δx = 20 km and Δx = 10 km.

5. Summary

A series of direct numerical experiments, combined with a bootstrap statistical analysis, have demonstrated that unresolved low-frequency variability causes significant uncertainties in the calculations of time-averaged values in a prototypical wind-driven ocean model. The results are consistent with more traditional estimates of the errors in moment estimates from observational data, but are based on simulations at least an order of magnitude longer than those previously reported in the literature. The calculations reported here are long enough to convincingly demonstrate the existence of a low-frequency plateau in the spectrum of total energy variability (below 0.1 cpy).

The results show that the uncertainty in the mean total energy decreases in a manner roughly proportional to the inverse square root of the averaging interval, with a "decorrelation timescale" that varied from 3 to 20 years, depending on the parameters of the model. This decorrelation timescale was almost independent of the magnitude of the wind stress curl, but was strongly dependent on the asymmetry of the driving wind field. The penetration scale and maximum transport obeyed similar statistical distributions, while the separation point location required only 2–3 year time averages to estimate accurately.

Application of this methodology to a study of the sensitivity of the model to various physical and numerical parameters has provided statistically robust estimates of the functional form of the sensitivities. Among the more interesting conclusions are the following:

- The location and variability of the separation point are both approximately linearly increasing functions of both wind stress magnitude and wind stress asymmetry.
- The penetration scale increases slightly less than linearly as the wind stress magnitude is increased and decreases slightly less than linearly as the wind stress asymmetry is increased.
- The fractional variability of the total energy is a very weak function of the wind stress magnitude once there is sufficient nonlinearity to generate eddies.

The results also suggest the difficulty of clearly identifying when (and by how much) solutions are different when only short runs are available. Based on the 100–200-year runs shown here, clear estimates of the dependencies of the mean total energy, mean separation point, and mean penetration scale have been obtained, but integration periods in the range of one decorrelation timescale might not even reliably determine the sign of the dependencies. In addition, the uncertainty of the estimates of standard deviations of model parameters are not always small even with the long integrations presented here.

The total energy of the model showed very weak dependence on both the grid spacing and the lateral hyperviscosity—both parameters whose "correct" values are beyond our current ability to simulate. There tended to be no statistically significant differences in the solutions with Δx = 20 km and Δx = 10 km, but there were strong and significant differences as the grid spacing was increased to 40 km. Both the penetration scale and separation point showed statistically significant variations in some cases as the lateral viscous parameter was varied.

The dynamical simplicity of the current model makes it unreasonable to project quantitative estimates of the averaging periods required for more dynamically complete models, but the methodology applied here may be applied to other models if there is a suspicion that the low-frequency variability is not well resolved. We note again that simple estimates of the decorrelation timescale are inherently biased downward for short runs (because of the removal of the sample mean rather than the global mean), and are therefore not reliable estimators for how well low-frequency variability is resolved in those cases.

The limitations of the current work suggest further studies in a number of areas—for example, examining the details of the low-frequency end of the spectrum via longer simulations (or ensembles of simulations); removing the constraint of quasigeostrophy in the governing equations; and removing the constraint of equivalent-barotropic dynamics. Unfortunately the computational costs of each of these additions to the complexity are multiplicative, so that future work will likely address these issues one at a time, rather than in one unified model. A discussion of the phenomenology of the low-frequency variability of this model will be the subject of another manuscript.

Acknowledgments. This worked was supported in part by Grant OCE-9206176 from the Ocean Sciences Division of the National Science Foundation. The computations reported here were made possible by a generous grant of computer resources from the University of Delaware Computing and Network Services.

APPENDIX

Definition of "Penetration Scale"

A detailed comparison of several definitions of penetration scale was made to attempt to understand statistical reliability of the measures. The definitions are of the type discussed in section 4a(1). The penetration scales defined by the eastward extent of the streamfunction will be denoted here by L_ψ, while the penetration scales defined by the eastward extent of the high-

velocity core of the free jet will be denoted by L_v. Both scales will have an additional subscript indicating the threshold value in percent.

As alternatives to these definitions, the first moments in x of the kinetic energy (KE) density and potential energy (PE) density distributions are also considered. In the context of a quasigeostrophic (QG) model these can be defined as

$$L_{KE} \equiv \frac{\iint (\nabla\psi \cdot \nabla\psi) x \, dxdy}{\iint (\nabla\psi \cdot \nabla\psi) dxdy}, \quad (13)$$

$$L_{PE} \equiv \frac{\iint (\psi^2) x \, dxdy}{\iint (\psi^2) dxdy}, \quad (14)$$

where the integrations are over the entire domain.

Moments based on perturbation mass are not considered, because the weight function is not positive definite. Also, moments based on absolute mass are not considered because these are not consistent with the quasigeostrophic model employed here. [In the QG formalism, one must substitute the reference layer thickness for the instantaneous layer thickness except when calculating the pressure gradients. The moments of the (constant) reference layer thickness are clearly not interesting dynamically.]

To analyze the relationships among the various definitions, as well as their sensitivities, a bootstrap approach was used, employing the 200 years of output from the reference case (run 104).

a. Dependence on threshold value

We begin by selecting a time-averaging period for the production of the "mean" streamfunctions. In the literature, time-averaging periods range from as short as approximately 5 years (Verron and LeProvost 1991; Schmitz and Holland 1982; Holland and Schmitz 1985) to 7 years (Barnier et al. 1991), to 10 years (Holland 1978). The longest averaging periods that have been used to date appear to be 20 and 40 years (Haidvogel et al. 1992). We choose an averaging interval of 5 years initially, and will discuss the effects of longer averaging periods later.

TABLE A1. Statistics of the penetration scale estimates based on 5-year time-averaged streamfunctions (upper four lines). The lower two lines are for the KE- and PE-weighted statistical moments based on instantaneous (5-day averaged) streamfunctions.

Measure	Mean (km)	Std dev (km)	Fractional variability
L_{v16}	1509	228	15%
L_{v50}	912	350	38%
$L_{\psi 20}$	2715	52	2%
$L_{\psi 50}$	1472	159	11%
L_{KE}	609	107	18%
L_{PE}	870	68	8%

TABLE A2. Correlation coefficients between selected pairs of streamfunction estimates as a function of averaging interval. Note that for the longer averaging periods only a few estimates are available, so the estimates of the coefficients may not be statistically significant.

Averaging period (years)	L_{v16} vs L_{v50}	$L_{\psi 20}$ vs $L_{\psi 50}$	L_{v16} vs $L_{\psi 20}$
5	0.69	0.88	0.15
10	0.59	0.87	0.58
20	0.80	0.97	0.37
40	−0.01	0.98	0.78
50	−0.67	0.98	0.76

With the choice of a 5-year averaging period, the 200 years of output thus provides us with 40 "independent" estimates of the mean streamfunction. These may not be independent in the statistical sense of being uncorrelated but are independent in the sense of not involving the reuse of any of the values in the calculation of more than one average.

Values of 20% and 50% were chosen as the thresholds for the calculation of L_ψ, and values of 16% and 50% were chosen as the thresholds for the calculation of L_v. The 16% threshold follows the definition in McWilliams et al. (1990). The other values were selected arbitrarily. Table A1 presents the mean, standard deviation, and fractional variability of each of the penetration scale estimates. Notable features of those results are the very large variability of L_{v50}, the very small variability of $L_{\psi 20}$, and the similar fractional variabilities of L_{v16} and L_{KE}. Before examining the results in more detail, the correlation coefficients of the estimates are calculated as a function of averaging period. The results are presented in Table A2. From the table, it is clear that the results of the streamfunction-based estimates, L_ψ, have a pattern variability that is very weakly influenced by the choice of threshold, while the results of the velocity-based estimates, L_v, have a pattern of variability that is very strongly influenced by the choice of threshold. It is further clear that the patterns of variabilities are quite different between the velocity-based and streamfunction-based estimators.

b. Time series

To compare the temporal patterns of variability of the L_ψ measures, the time series of the values based on the 5-year mean streamfunctions is plotted in Fig. A1, along with L_{PE} for comparison. Each of the three curves has been normalized by its mean to facilitate compar-

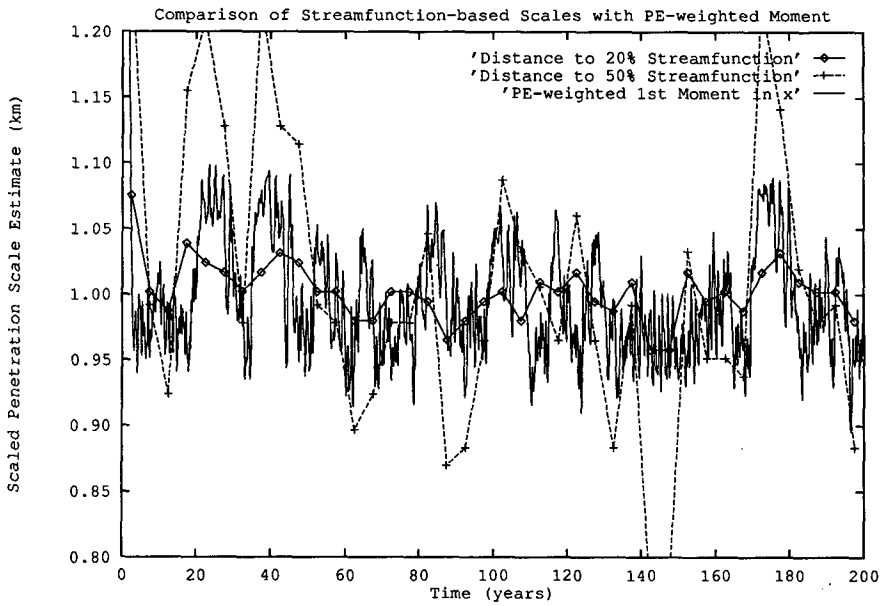

FIG. A1. Comparison of penetration scale estimates based on the eastward extent of the 20% streamfunction contours, the 50% streamfunction contour, and the first moment in x of the PE density distribution. All three curves have been normalized by their respective mean values.

ison and to show more clearly how the fractional variability differs among the three measures. The variability of these curves does not correlate well with any of the other major statistics of the system (e.g., PE, KE, total energy, total enstrophy, or peak streamfunction).

The results for the velocity-based penetration scale estimates, L_v, are more satisfying. The time series of L_{v16}, L_{v50}, and L_{KE} are presented in Fig. A2. There is a good visual correspondence between the major peaks and valleys of the signals, particularly between L_{v16}

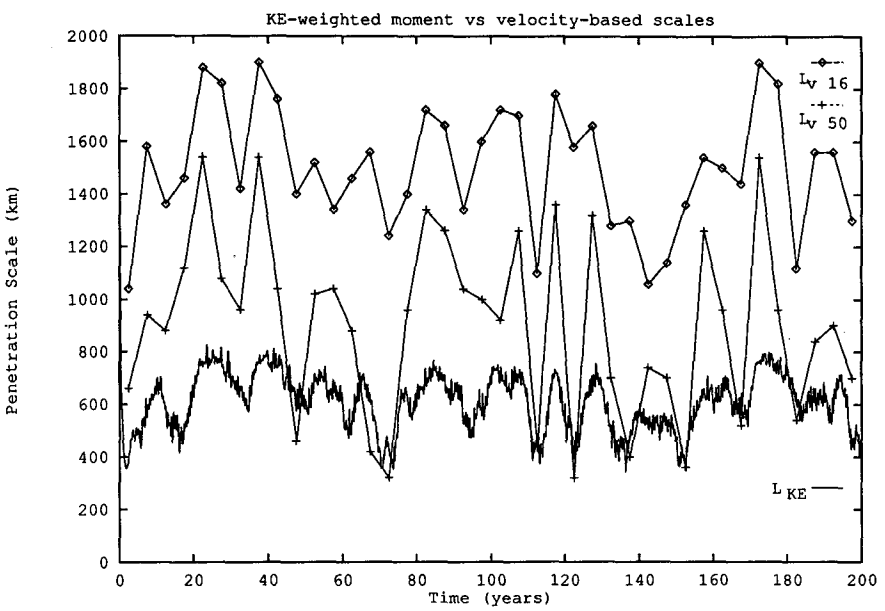

FIG. A2. Comparison of velocity-based penetration scale estimates with the first moment in x of the KE distribution.

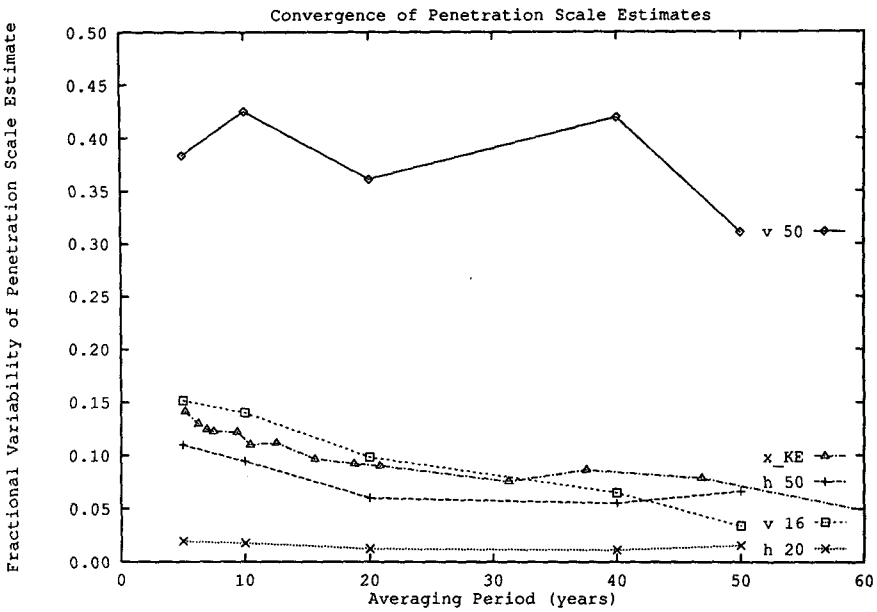

FIG. A3. Fractional variability of the penetration scale estimates as a function of the averaging interval. Only L_{v16} and L_{KE} appear to be converging to a constant value for long averaging periods.

and L_{KE}. Noting that L_{v16} and L_{KE} have similar fractional variabilities, we expect that the normalized series will almost overlap, as they do (not shown). The L_{v16} series based on longer time averages of the streamfunction field are not shown here but do follow the low-frequency variability of the L_{KE} curve visually.

Unlike the case with L_{PE}, the L_{KE} estimator is very highly correlated with some important statistical measures of the system, in this case, the total energy (which is dominated by the potential energy). The correlation coefficient between L_{KE} and total energy is 0.935 for the last 190 years of the series. In light of Fig. A2, it is not surprising that L_{v16} is also correlated very well with the total energy time series. It is not clear whether this is a general conclusion or an artifact of the reduced-gravity approximation of the model used here.

c. *Dependence on averaging interval*

The details of the dependence of the various integral measures of the model on the averaging interval have been dealt with in greater detail earlier, but one figure will be presented here. Fig. A3 shows the fractional variability of the L_{ψ}, L_{v}, and L_{KE} penetration scale estimators as a function of the length of the averaging interval. One might expect that a "good" measure of the penetration scale of the system should have the property that the differences between the estimates get arbitrarily small as the averaging period is increased. This would be reflected by a fractional variability that smoothly decreased to (near) zero for long averaging periods. It is important to note that only the curves for L_{v16} and L_{KE} exhibit this behavior. The curves for $L_{\psi 20}$ and $L_{\psi 50}$ both exhibit small fractional variability, but both *increase* somewhat for the longest averaging interval, and $L_{\psi 20}$, in particular, does not decrease significantly as the averaging interval increases from 5 to 40 years.

Of the four estimators patterned after common usage, only one set of parameters led to results that appeared consistent with standard statistical moments and with convergence to an asymptotic value for long averaging periods. To avoid the uncertainties associated with the averaging periods and adjustable parameters of these definitions, the use of the first moment in x of the KE density distribution is recommended for estimating the free-jet penetration scale in future work. It has the advantages of a clear and unambiguous definition, a freedom from arbitrary user-selectable parameters, and it does not require time-averaged streamfunctions in order to make sense. The time series of the resulting estimates can then be averaged as desired.

REFERENCES

Adamec, D., 1988: Numerical simulations of the effect of seamounts and vertical resolution on strong ocean flows. *J. Phys. Oceanogr.*, **18**, 258–269.

——, 1989: Predictability of quasi-geostrophic ocean flow: Sensitivity to varying model vertical resolution. *J. Phys. Oceanogr.*, **19**, 1753–1764.

Arakawa, A., 1966: Computational design for long-term numerical integration of the equations of fluid motion: Two-dimensional incompressible flow. Part I. *J. Comput. Phys.*, **1**, 119–143.

Barnier, B., B. Lien-Hua, and C. LeProvost, 1991: On the catalytic role of high baroclinic modes in eddy-driven large-scale circulations. *J. Phys. Oceanogr.*, **21,** 976–997.

Bryan, K., 1963: A numerical investigation of a non-linear model of a wind-driven ocean. *J. Atmos. Sci.*, **20,** 594–606.

Chassignet, E., and P. R. Gent, 1991: The influence of boundary conditions on midlatitude jet separation in ocean numerical models. *J. Phys. Oceanogr.*, **21,** 1290–1299.

Flierl, G. R., and J. C. McWilliams, 1977: On the sampling requirements for measuring moments of eddy variability. *J. Mar. Res.*, **35,** 797–820.

Haidvogel, D. B., 1979: A discussion of certain modeling factors which influence the result of eddy-resolving ocean circulation studies. *Dyn. Atmos. Oceans,* **3,** 181–190.

——, J. C. McWilliams, and P. R. Gent, 1992: Boundary current separation in a quasigeostrophic, eddy-resolving ocean circulation model. *J. Phys. Oceanogr.*, **22,** 882–902.

Holland, W., and W. Schmitz, 1985: Zonal penetration scale of model midlatitude jets. *J. Phys. Oceanogr.*, **15,** 1859–1875.

Holland, W. R., 1973: Baroclinic and topographic influences on the transport in a western boundary current. *Geophys. Fluid Dyn.*, **4,** 187–210.

——, 1978: The role of mesoscale eddies in the general circulation of the ocean—numerical experiments using a wind-driven quasi-geostrophic model. *J. Phys. Oceanogr.*, **8,** 363–392.

——, and L. B. Lin, 1975: On the generation of mesoscale eddies and their contribution to the oceanic general circulation. II: A parameter study. *J. Phys. Oceanogr.*, **5,** 658–669.

Marshall, D., and J. Marshall, 1992: Zonal penetration scale of midlatitude oceanic jets. *J. Phys. Oceanogr.*, **22,** 1018–1032.

McCalpin, J. D., 1987: On the adjustment of azimuthally perturbed vortices. *J. Geophys. Res.*, **92,** 8213–8225.

McWilliams, J. C., 1977: A note on a consistent quasigeostrophic model in a multiply-connected domain. *Dyn. Atmos. Oceans,* **1,** 427–441.

——, N. J. Norton, P. R. Gent, and D. B. Haidvogel, 1990: A linear balance model of wind-driven, midlatitude ocean circulation. *J. Phys. Oceanogr.*, **20,** 1349–1378.

Rhines, P. B., and R. Schopp, 1991: The wind-driven circulation: Quasi-geostrophic simulations and theory for nonuniform winds. *J. Phys. Oceanogr.*, **21,** 1438–1469.

Schmitz, W. J., and W. R. Holland, 1982: A preliminary comparison of selected numerical eddy-resolving general circulation experiments with observations. *J. Mar. Res.*, **40,** 75–117.

Veronis, G., 1966: Wind-driven ocean circulation. Part 2: Numerical solutions of the non-linear problem. *Deep-Sea Res.*, **13,** 31–55.

Verron, J., and C. LeProvost, 1991: Response of eddy-resolved general circulation numerical models to asymmetrical wind forcing. *Dyn. Atmos. Oceans,* **15,** 505–533.

——, ——, and W. R. Holland, 1987: On the effects of a midocean ridge on the general circulation: Numerical simulations with an eddy-resolved ocean model. *J. Phys. Oceanogr.*, **17,** 301–312.

Wunsch, C., 1992: Decade-to-century changes in the ocean circulation. *Oceanography,* **5,** 99–106.